

Improving resolution in microscopic holography by computationally fusing multiple, obliquely illuminated object waves in the Fourier domain

Jeffery R. Price, Philip R. Bingham, and C. E. Thomas, Jr.

We present a computational method to increase the effective NA of a holographic microscopy system operating in air. Our optical system employs a reflection Mach-Zender architecture and computational reconstruction of the full complex (phase and amplitude) wavefront. Based on fundamental diffraction principles, different angles of incident illumination result in different diffracted orders of the object wave being imaged. We record, store, and computationally recombine these object waves to expand the spatial frequency response. Experimental results demonstrate an improvement in the effective NA of our system from 0.59 to 0.78. © 2007 Optical Society of America

OCIS codes: 090.1760, 090.2880.

1. Introduction

The idea of computer-based hologram reconstruction was proposed over four decades ago.¹ Dramatic increases in both computing power and digital imaging devices in intervening years, however, have made practical applications a reality. For example, Takeda *et al.*² introduced a fast Fourier transform (FFT) method for topography and interferometry using a digital imaging device. Schnars³ showed how to computationally reconstruct both intensity and phase from digitally sampled holographic interferometry images that were captured with a CCD imager. Cuche *et al.*⁴ demonstrated the recovery of both phase and magnitude information for holographic microscopy using the Fresnel approximation, FFT processing, and a Mach-Zender architecture similar to what we use in this work.

Our current application domain is semiconductor inspection.⁵⁻⁷ In this regard, intensity imaging alone is often not effective enough at detecting critical semiconductor defects. By employing holography to

measure phase information, differences in material and/or height can be detected that cause little or no change in the image intensity. Spatial resolution, however, is limited by the optics as well as the need to operate in air to preserve the semiconductor surface. Though theoretically limited to a NA of 1.0 in air, achieving a high NA without significant aberrations is challenging considering the coherent light sources required for interferometry.

In this work we describe a technique for increasing the effective NA of a microscopic holography system operating in air. The system we employ is based upon the Mach-Zender architecture and uses image plane recording. An angle is introduced between the reference and the target beam to create linear fringes and we use Fourier-domain reconstruction as in Takeda *et al.*² The specific contributions of this paper are

- Fourier and spatial domain models relating reconstructed object waves in microscopic holography that have been acquired with different illumination angles,
- A method for estimating parameters that might vary between reconstructed object waves acquired at different times under different illumination angles,
- A technique to computationally recombine multiple reconstructed object waves, acquired under a variety of illumination angles, that increases spatial resolution, and
- Experimental verification of the proposed technique demonstrating an improvement in our system from a physical NA of 0.59 to an effective NA greater than 0.78.

J. R. Price (pricejr@ornl.gov) and P. R. Bingham are with the Image Science and Machine Vision Group, Oak Ridge National Laboratory, P.O. Box 2008, Oak Ridge, Tennessee 37831, USA. C. E. Thomas, Jr. (thomasce2@att.net) is with Third Dimension Technologies LLC, 3601 Bluff Point Drive, Knoxville, Tennessee 37920, USA.

Received 21 August 2006; revised 6 October 2006; accepted 26 October 2006; posted 26 October 2006 (Doc. ID 74143); published 2 February 2007.

0003-6935/07/060827-07\$15.00/0

© 2007 Optical Society of America

The remainder of this paper is organized as follows. In Section 2 we review some fundamental principles of optical resolution as well as the basic equations of holography in the context of our optical system. In Section 3 we introduce our technique for computationally combining multiple complex wavefronts—acquired under different illumination angles—to produce a higher-resolution resultant image. We demonstrate our technique in Section 4 by using a semiconductor test wafer that contains a pattern beyond the optical resolution of our system. We close in Section 5 with some summary comments.

2. Principles

First, in Subsection 2.A below, we review some fundamental principles relating resolution to diffraction and NA. Next, in Subsection 2.B, we describe the principles of holography used in this paper and introduce the requisite notation.

A. Diffraction, Numerical Aperture, and Resolution

To better elucidate the contributions of this paper, we first recall some fundamentals of diffraction, NA, and resolution. For a given microscope objective the numerical aperture, NA, is defined as $NA = n \sin \theta$, where n is the index of refraction of the medium in which the objective is operating, and θ is the half-angle of the maximal cone of light that the objective can receive. As we are operating in air, we will assume $n = 1$ henceforth. For a repeating pattern (e.g., a grating) of period d , the angle of diffracted order M , ϕ_M , is related to the incident angle of the illumination, ϕ_i by the well-known grating equation

$$\sin \phi_M + \sin \phi_i = M \frac{\lambda}{d}, \quad (1)$$

where λ is the wavelength of light. According to Abbe,⁸ we must observe at least the zero and first diffracted orders to accurately resolve a repeating pattern. Combining the expression for NA and the grating equation, with $\phi_i = 0^\circ$ and $M = 1$, the resolution limit (minimal period) for repeating lines in air is given by

$$d_{\min} = \lambda/NA. \quad (2)$$

Consider Fig. 1(a), for example, with normal illumination ($\sin \phi_i = 0$) where both the +1 and -1 diffracted orders fall outside the receiving cone of the objective; this pattern cannot be resolved. In Fig. 1(b), however, we illustrate oblique illumination that results in the objective receiving both the 0 and +1 diffracted orders, though not the -1 order. If we were to consider the mirror of Fig. 1(b), with the opposite angle of incident illumination, the objective would receive the -1 order but not the +1 order. An effective increase in the NA could be achieved if the information from these two illumination conditions could be combined; that is our goal in this paper.

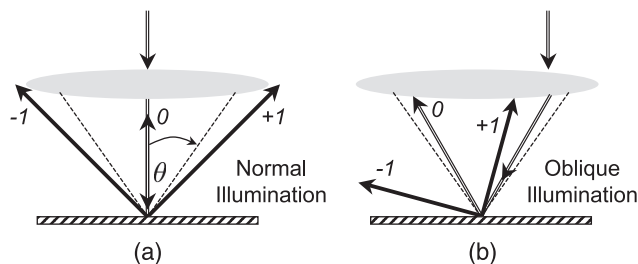


Fig. 1. Relationship between NA, resolution, diffracted orders, and oblique illumination. The acceptance cone of half-angle θ is indicated by the dashed lines. Illumination and zero-order diffraction are indicated with double lines, while the first diffracted orders are indicated with solid single lines. (a) Illumination is normally incident upon the specimen, and both the +1 and -1 diffracted orders are outside the acceptance cone. (b) Oblique illumination causes the +1 diffracted order to fall within the acceptance cone.

B. Microscopic Holography

The holographic imaging system we employ, as illustrated in the schematic of Fig. 2, is based upon the Mach-Zehnder interferometer. For this system, the field intensity at the CCD camera is given by the basic hologram equation.⁹ Assuming a unity-normalized incident amplitude, this can be written

$$I_{\text{CCD}}(x) = 1 + |a(x)|^2 + 2a(x)\cos[2\pi c^T x + \phi(x)], \quad (3)$$

where $a(x)$ is the amplitude component, which is a function of the object reflectivity, and $\phi(x)$ is the phase component, which is a function of the object topography and the material's complex index of refraction. The index x is a two-vector, $x = (x_1 \ x_2)^T$, where $(\cdot)^T$ represents the transpose. We refer to the $c = (c_1 \ c_2)^T$ term as the carrier frequency, which is a function of the relative angle between the object and the reference waves at the CCD imaging plane. A small region of an example hologram image is shown in Fig. 3; note the diagonal fringes that correspond to the $\cos(\cdot)$ term above.

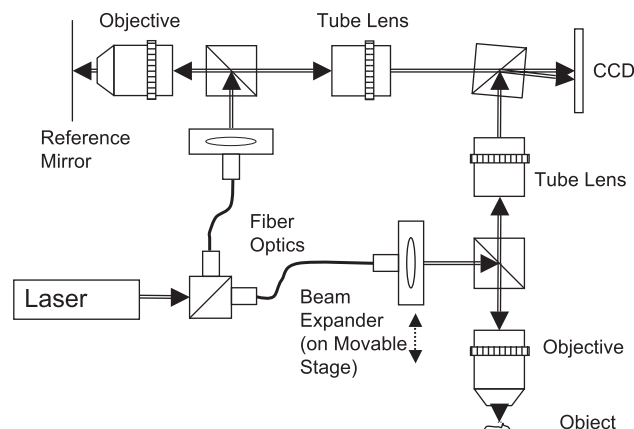


Fig. 2. Simplified schematic of digital holography system used in our experiments. Note that the beam expander is mounted on a bidirectional motorized stage.

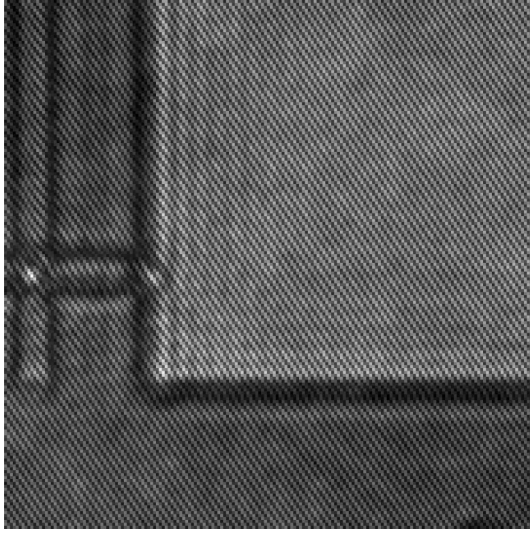


Fig. 3. Small region ($21.6 \mu\text{m} \times 21.6 \mu\text{m}$) of an example hologram image. Note the fringe pattern, aligned diagonally from the top left to the bottom right that is a result of interference between the object and reference waves.

The quantity we desire to measure in this process is the true object wave, $f(x)$, which is defined by

$$f(x) = a(x)e^{j\phi(x)}. \quad (4)$$

Our observation of this object wave, however, is resolution limited by the optical components of the system. Explicitly indicating some potential sources of variation, the observed object wave component, $\tilde{f}(x)$, of a recorded hologram in the form of Eq. (3) can be written

$$\tilde{f}(x) = \mu a(x) \cos[2\pi c^T x + \gamma + \phi(x)] * \tilde{w}(x), \quad (5)$$

where the “*” operator indicates convolution, γ is the initial phase offset, μ is the fringe contrast (which may vary between acquisitions with random fluctuations of illumination intensity), and

$$\tilde{w}(x) = w(x)e^{j2\pi c^T x} \quad (6)$$

represents the point spread function (PSF) of the objective optics, $w(x)$, modulated to the carrier frequency. Assuming the absence of aberrations, $w(x)$ is defined by the NA of the objective optics. The Fourier transform $W(u)$ of $w(x)$ has a flat, circular passband centered on $u = 0$ (assuming normal illumination). The radial bandwidth of this aperture in the Fourier plane corresponds to the resolution limit of the holographic imaging system.

In Fig. 4, we show the log-magnitude of the FFT for an example hologram in the form of Eq. (3). The center bright region represents the autocorrelation, denoted by $1 + |a(x)|^2$ in Eq. (3). The bright regions in the upper-right and lower-left quadrants are the sidebands and correspond to the $\cos[2\pi c^T x + \phi(x)]$

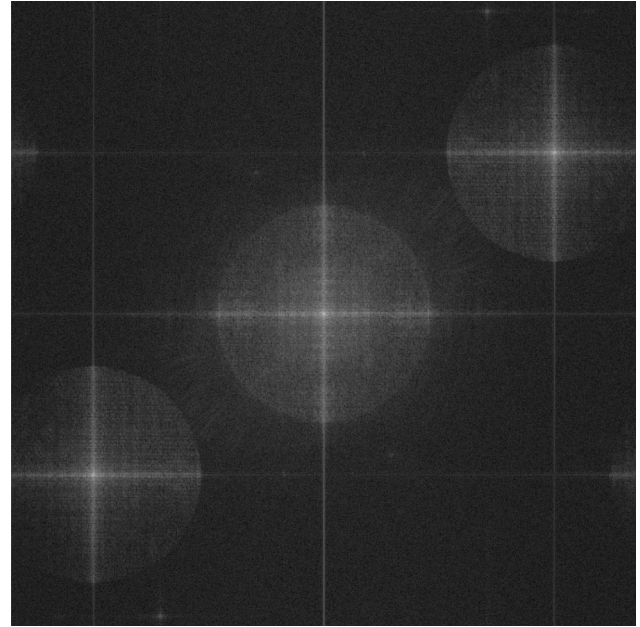


Fig. 4. Log-magnitude FFT of an example hologram. The center corresponds to the autocorrelation term while the upper-right and lower-left sidebands result from the fringe pattern. The object wave is reconstructed from just one of the sidebands.

term from Eq. (3) that is a result of the interfering object and reference waves. In this example, normal illumination was used resulting in the sidebands being centered on the carrier frequency, c , which is represented by the bright center dot in each sideband. The complex object wave is encoded in each sideband; it is reconstructed from one of the sidebands using appropriate FFT-domain processing.⁷ Since the quantity of interest is fully represented by a single sideband, we will henceforth display only a single sideband in FFT illustrations.

3. Improving Resolution by Combining Obliquely Illuminated Object Waves

We now turn our attention to the central focus of this paper. Recalling the discussion of Subsection 2.A and the system schematic of Fig. 2, we can simply achieve and accurately control oblique illumination in our system by translating the illumination arm relative to the beam splitter, as illustrated in Fig. 5. In Fig. 6 we show log-magnitude FFTs of the sideband components for a test object under different oblique illumination conditions. Noting that zero spatial frequency is represented by the brightest spot (the carrier frequency), it is evident from this figure—and expected from the discussion in Subsection 2.A above—that each differently illuminated hologram observes a different region (with some overlap) of the object wave’s Fourier components (diffracted orders). Our goal is to combine these observations to produce a higher-resolution object wave representation.

When multiple holograms of a given object are recorded at different times with different illumination angles, several quantities from Eq. (5) can vary be-

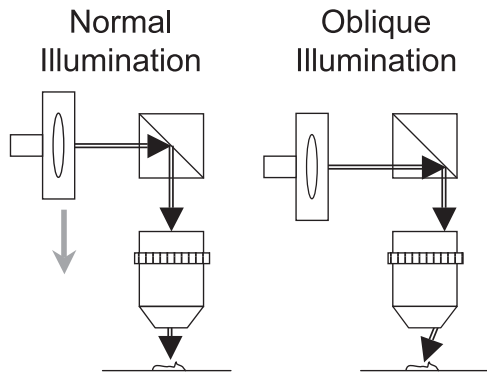


Fig. 5. Recalling the system schematic in Fig. 2, the motorized stage can be used to move the beam expander to achieve and accurately control oblique illumination.

tween successive shots. These include fringe contrast (μ), initial phase offset (γ), and carrier frequency (c). Additionally, it is possible that physical limitations (e.g., vibration and stage drift) can cause the object to shift spatially with respect to the imaging system. We represent these potential sources of disturbance as follows. Suppose that $N + 1$ holograms of a given object have been recorded; the object wave component of the k th hologram is given by

$$h_k(x) = \mu_k a(x + \Delta x_k) \cos[2\pi c_k^T x + \gamma_k + \phi(x + \Delta x_k)] * \tilde{w}_k(x), \quad (7)$$

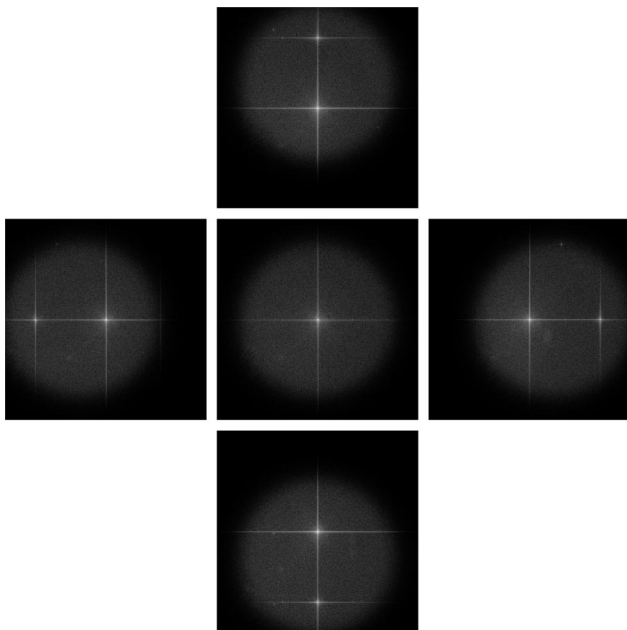


Fig. 6. Log-magnitude sideband FFTs of a test object under different oblique illuminations (normal illumination is shown in the center). All images are centered on the carrier frequency (the bright spot in each square image center). Data were acquired from a sample with a grating-like pattern beyond the optical resolution of the system. Note the appearance of the first diffracted order bright spots in the oblique-illumination examples. (See Section 4 for details.)

for $k = 0, \dots, N$, where Δx_k indicates possible spatial shifting and where

$$\tilde{w}_k(x) = [w_k(x)]e^{j2\pi c_k^T x} = [w(x)e^{j2\pi q_k^T x}]e^{j2\pi c_k^T x}. \quad (8)$$

Regarding Eq. (8), we note that the Fourier transform, $W_k(u)$, of k th effective aperture, $w_k(x)$, is just $W(u - q_k)$. In other words, in the Fourier domain, we represent the k th obliquely illuminated aperture as the normally illuminated aperture ($k = 0$) shifted by q_k . We assume henceforth that $k = 0$ always corresponds to normal illumination.

The k th observation, $g_k(x)$, of the high-resolution object wave, $f(x)$, is reconstructed by modulating $h_k(x)$ by the estimated carrier frequency and low-pass filtering the result. This yields

$$g_k(x) = \mu_k e^{j\gamma_k} e^{j2\pi \Delta c_k^T x} [a(x + \Delta x_k) e^{j\phi(x + \Delta x_k)}] * w_k(x) e^{j2\pi \Delta c_k^T x} \\ = \mu_k e^{j\gamma_k} e^{j2\pi \Delta c_k^T x} [f(x + \Delta x_k)] * w_k(x) e^{j2\pi \Delta c_k^T x}, \quad (9)$$

where Δc_k indicates potential error in the estimation of the carrier frequency. Equation (9) can be expressed in the Fourier domain as

$$G_k(u) = \mu_k e^{j\gamma_k} e^{-j2\pi \Delta c_k^T \Delta x_k} e^{j2\pi u^T \Delta x_k} F(u - \Delta c_k) W_k(u - \Delta c_k). \quad (10)$$

We now consider the computation of an optimal estimate of the true object wave using the set of observations described by Eqs. (9) and (10) for $k = 0, \dots, N$.

A. Normalizing Fringe Contrast and Phase Offset

We first assume that any spatial shift between shots is negligible, so that $\Delta x_k = 0$. Additionally, we assume that carrier error is negligible, so that $\Delta c_k = 0$. In practice, these assumptions are met by appropriate preprocessing that includes subpixel image registration and sub-bin location of the carrier frequency. Under these conditions, we may then rewrite Eqs. (9) and (10) more simply as

$$g_k(x) = \mu_k e^{j\gamma_k} f(x) * w_k(x), \quad (11)$$

$$G_k(u) = \mu_k e^{j\gamma_k} F(u) W_k(u), \quad (12)$$

respectively.

To address variations in fringe contrast and phase offset, we first define images $g_{k,0}(x)$ and $g_{0,k}(x)$ as follows. The image $g_{k,0}(x)$ is constructed from $g_k(x)$ by keeping only the frequencies common to both $g_k(x)$ and $g_0(x)$. Similarly, the image $g_{0,k}(x)$ is constructed by keeping only the frequencies of $g_0(x)$ common to both $g_0(x)$ and $g_k(x)$. The region of common frequencies can be visualized as the product of $W_0(u)$ and $W_k(u)$ in the Fourier domain, as illustrated in Fig. 7. Recalling Eq. (11), $g_{k,0}(x)$ and $g_{0,k}(x)$ are defined mathematically by

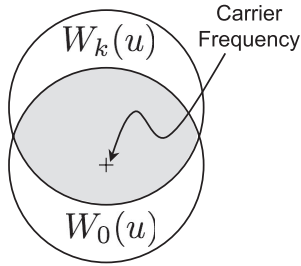


Fig. 7. Shaded region represents the common frequency content for $g_k(x)$ and $g_0(x)$ used when estimating fringe contrast and phase offset. In the Fourier domain this region is defined by the product $W_0(u)W_k(u)$.

$$\begin{aligned} g_{k,0}(x) &= \mathcal{F}^{-1}\{G_k(u)W_0(u)\} \\ &= \mathcal{F}^{-1}\{\mu_k e^{j\gamma_k} F(u)W_k(u)W_0(u)\} \\ &= \mu_k e^{j\gamma_k} f(x) * w_k(x) * w_0(x), \end{aligned} \quad (13)$$

$$\begin{aligned} g_{0,k}(x) &= \mathcal{F}^{-1}\{G_0(u)W_k(u)\} \\ &= \mathcal{F}^{-1}\{\mu_0 e^{j\gamma_0} F(u)W_0(u)W_k(u)\} \\ &= \mu_0 e^{j\gamma_0} f(x) * w_0(x) * w_k(x), \end{aligned} \quad (14)$$

for $k = 1, \dots, N$, where \mathcal{F} indicates the Fourier-transform operation.

Once the images of Eqs. (13) and (14) have been constructed, we compute the complex ratio image:

$$\chi_k(x) = \frac{g_{k,0}(x)}{g_{0,k}(x)} \approx \frac{\mu_k e^{j\gamma_k}}{\mu_0 e^{j\gamma_0}}. \quad (15)$$

Without any noise or disturbance terms, $\chi_k(x)$ would equal $(\mu_k e^{j\gamma_k})/\mu_0 e^{j\gamma_0}$ for all x . Considering noise, however, we compute

$$\hat{\chi}_k = \varepsilon_x\{\chi_k(x)\}, \quad (16)$$

where $\varepsilon_x\{\cdot\}$ indicates the sample mean. Note that

$$\begin{aligned} |\hat{\chi}_k| &\approx \frac{\mu_k}{\mu_0}, \\ \frac{\hat{\chi}_k}{|\hat{\chi}_k|} &\approx \frac{e^{j\gamma_k}}{e^{j\gamma_0}}. \end{aligned}$$

We then multiply each object wave $g_k(x) \leftrightarrow G_k(u)$ by $(\hat{\chi}_k)^{-1}$ to yield

$$(\hat{\chi}_k)^{-1} g_k(x) \approx \mu_0 e^{j\gamma_0} f(x) * w_k(x), \quad (17a)$$

or in the Fourier domain,

$$(\hat{\chi}_k)^{-1} G_k(u) \approx \mu_0 e^{j\gamma_0} F(u)W_k(u). \quad (17b)$$

After this normalization, each object wave is scaled by (approximately) the same complex constant, $\mu_0 e^{j\gamma_0}$. We can therefore drop this constant from further notation and just write

$$g_k(x) \approx f(x) * w_k(x), \quad (18)$$

$$G_k(u) \approx F(u)W_k(u), \quad (19)$$

where, for notational convenience, we have eliminated the common normalization factor $(\hat{\chi}_k)^{-1}$. Equations (18) and (19) serve as the starting point for estimating the high resolution image as will be described in Subsection 3.B.

We also tested three alternate approaches for estimating fringe contrast and/or phase offset. These included (a) a method similar to that described above, but in the frequency domain; (b) using only the carrier frequency FFT ratios, i.e., $H_k(c_k)/H_0(c_0)$ where $H_k(u)$ is the FFT of the k th hologram; and (c) using the ratios of the FFT value at the carrier to the FFT value at zero frequency, i.e., $H_k(c_k)/H_0(0)$ (this gives only fringe contrast). Though these alternative methods are more computationally efficient (requiring less FFTs), none proved as robust as the method described above in detail.

B. Estimating the Object Wave

We employ a linear, minimum mean-square error (LMMSE) estimator to compute the object wave. Recalling Eq. (19), suppose that we are examining a given frequency bin in the FFT domain so that u is fixed and can be dropped from the notation. For the given bin, we write

$$G_k = W_k F + N_k, \quad (20)$$

where N_k represents observation noise. For the LMMSE estimate, we seek coefficients $\{\beta_k\}_{k=0}^N$ to satisfy

$$\boldsymbol{\beta} = \arg \min_{\boldsymbol{\beta}} \varepsilon\{|F - \hat{F}|^2\}, \quad (21)$$

where $\boldsymbol{\beta}$ indicates the $(N + 1)$ -point column vector whose k th element is β_k , $\varepsilon\{\cdot\}$ indicates the expected value, and the estimate \hat{F} is given by

$$\hat{F} = \sum_{k=0}^N \beta_k G_k. \quad (22)$$

Assuming that the observation noise between successive image captures is uncorrelated, i.e., that

$$\varepsilon\{N_l N_k^*\} = \begin{cases} \sigma_N^2 & \text{if } l = k \\ 0 & \text{if } l \neq k \end{cases}$$

the estimator coefficients are given by

$$\boldsymbol{\beta} = \left(\mathbf{M}(\mathbf{W}) + \frac{\sigma_N^2}{\sigma_F^2} \mathbf{I} \right)^{-1} \mathbf{W}, \quad (23)$$

where \mathbf{W} is the $(N + 1)$ -point vector defined by $\{\mathbf{W}\}_k = W_k$, the $(N + 1) \times (N + 1)$ matrix $\mathbf{M}(\mathbf{W})$ is defined

by $\{M(\mathbf{W})\}_{m,n} = W_m W_n$, and $\sigma_F^2 = \varepsilon\{FF^*\}$ is the signal power for the given frequency bin. Letting

$$\mathcal{H} = \frac{\sigma_N^2}{\sigma_F^2} \quad (24)$$

represent the ratio of noise power to signal power, solving Eq. (23) yields

$$\beta_k = \frac{W_k}{(\sum_{k=0}^N W_k^2) + \mathcal{H}}, \quad (25)$$

for $k = 0, \dots, N$. Note that \mathcal{H} is just a regularization term.

In summary, we compute the estimated high-resolution object wave by fusing the observed low-resolution object waves in the FFT domain according to

$$\hat{F}(u) = \sum_{k=0}^N \beta_k(u) G_k(u), \quad (26)$$

where

$$\beta_k(u) = \frac{W_k(u)}{(\sum_{k=0}^N W_k^2(u)) + \mathcal{H}(u)}. \quad (27)$$

Note that we have now explicitly indicated the dependence on the frequency index u . In our current implementation, the regularization term $\mathcal{H}(u)$ is left constant across all frequencies u and its value is chosen to match the system characteristics.

4. Experimental Results

In this section we provide experimental results demonstrating the effectiveness of the proposed technique. Our holography system, as illustrated in the schematic of Fig. 2, employs a $\lambda = 532$ nm laser and a $100\times$ objective with $NA = 0.59$. The CCD is a 1024×1024 array with $12.0 \mu\text{m}$ square pixels yielding an effective pixel size of 120 nm and a field-of-view of approximately $123 \mu\text{m} \times 123 \mu\text{m}$ when combined with the $100\times$ magnification. Recalling Eq.

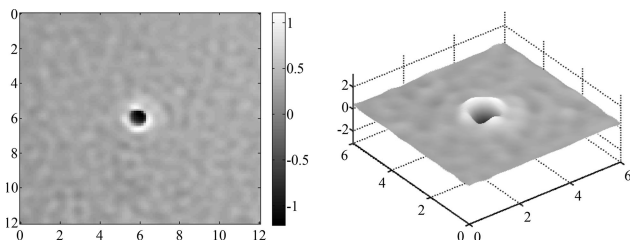


Fig. 8. Reconstructed phase of semiconductor test wafer from a single hologram using normal illumination. Though the defect in the center is detectable, there is no evidence of the beyond-resolution 680 nm repeated pattern. The x and y scales are in micrometers, grayscale and height are in radians, where 2π corresponds to $\lambda = 532$ nm.

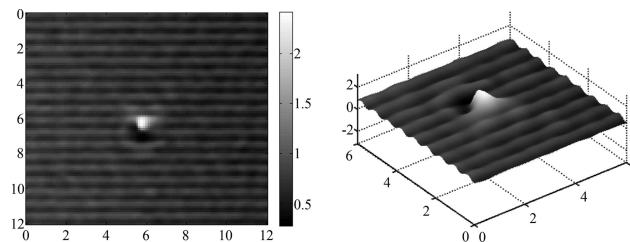


Fig. 9. Reconstructed phase of semiconductor test wafer using (vertical) oblique illumination. Note that horizontal component of the 680 nm pattern is now apparent owing to the principles discussed in Subsection 2.A. The x and y scales are in micrometers, grayscale and height are in radians, where 2π corresponds to $\lambda = 532$ nm.

(2), we note that the Abbe resolution limit for our system is $d_{\min} = 532 \text{ nm}/0.59 = 902 \text{ nm}$.

For our experiments, we imaged a semiconductor test wafer containing a 2D repeated pattern of period 680 nm in both the horizontal and vertical directions. This pattern is composed of 220 nm diameter vias (voids), 1500 nm deep, etched in SiO_2 . We note that the 680 nm period is well below the resolution limit of 902 nm. We used simple $\arctan(\cdot)$ phase reconstruction with no unwrapping (most optical path lengths in our data are within a 532 nm range). In Fig. 8 we show the reconstructed phase front for a single hologram with normal illumination. The dark spot in the center of the image corresponds to a single defective via that is partially filled with SiO_2 (i.e., the etching was incomplete). Though this defect can be detected, the 680 nm periodic pattern is not resolved. In Fig. 9, however, we show the reconstructed phase for a single hologram acquired with oblique illumination. As represented earlier in Fig. 1, the oblique illumination allows us to acquire one of the first diffracted orders, and the periodic pattern (in the horizontal direction) can be seen. We acquired five different holograms for this test wafer, one with normal illumination and four with oblique illumination; the log-magnitude FFTs of the corresponding sidebands were shown

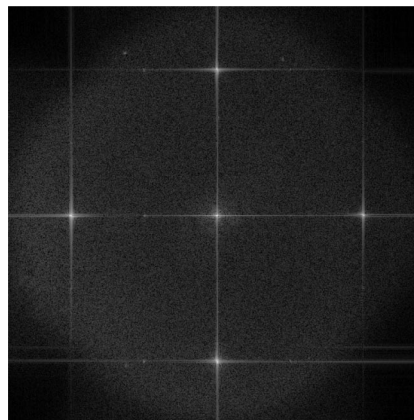


Fig. 10. Log-magnitude of computationally combined FFTs, computed using the method described in Section 3. Note the presence of the positive and negative first diffracted orders in both the horizontal and vertical directions.

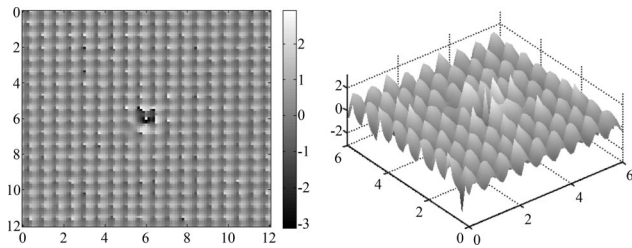


Fig. 11. Phase of semiconductor test wafer computed from computationally combining five reconstructed object waves (one normally illuminated and four obliquely illuminated) as described in Section 3. Note that the 680 nm pattern can be resolved in both the horizontal and vertical directions. The x and y scales are in micrometers, grayscale and height are in radians, where 2π corresponds to $\lambda = 532$ nm.

previously in Fig. 6. Using the method of Section 3, we combined these FFTs, and the result is shown in Fig. 10. It is evident in the figure that both diffracted orders in both directions are present. We show in Fig. 11 the phase of the corresponding object wave, where the 680 nm pattern is resolved in both the horizontal and vertical directions. The regularization parameter, $\mathcal{H}(u)$ from Eq. (27), was set to a constant value of 0.01 for these experiments, and the PSF of the optical system [$W(u)$ from Subsection 2.B] was modeled in the discrete Fourier domain with an eighth-order, radially symmetric Butterworth filter.¹⁰

With the capability of resolving 680 nm repeated patterns, the effective numerical aperture, NA_e , has been increased to

$$NA_e \geq 0.782 (\approx 532 \text{ nm}/680 \text{ nm}) \quad (28)$$

from the objective NA of 0.59. This corresponds to an effective increase of 16° in the opening angle, from 36° to approximately 52° . Recalling the discussion from Subsection 2.A as well as Fig. 1, the potential resolution improvement afforded by the proposed technique is represented by the increase in the effective opening angle. Since the zero diffracted order must always be passed, it is easy to see that the increase in effective opening angle is limited to the lesser of twice the opening angle of the objective or 90° . Hence with objective optics whose opening angle is $>45^\circ$ (i.e., $NA > 0.707$), it is practically possible with this technique to achieve very close to the maximum theoretical NA of 1.0 in air.

5. Conclusions

We have presented a method for increasing the resolution of a microscopic holography system operating

in air. Several holograms are recorded using normal and oblique illumination on the object, resulting in different Fourier regions of the object wave being imaged. The reconstructed object waves are then computationally recombined in the FFT domain resulting in a new object wave estimate with higher resolution. Experimental results on a gratinglike pattern with a 680 nm period demonstrated an increase in the effective NA of our system from 0.59 to greater than 0.78.

Prepared by Oak Ridge National Laboratory, managed by UT-Battelle, LLC, for the U.S. Department of Energy under contract DE-AC05-00OR22725.

References

1. J. Goodman and R. Lawrence, "Digital image formation from electronically detected holograms," *Appl. Phys. Lett.* **11**, 77–79 (1967).
2. M. Takeda, H. Ina, and S. Kobayashi, "Fourier-transform method of fringe-pattern analysis for computer-based topography and interferometry," *J. Opt. Soc. Am.* **72**, 156–160 (1982).
3. U. Schnars, "Direct phase determination in hologram interferometry with use of digitally recorded holograms," *J. Opt. Soc. Am. A* **11**, 2011–2015 (1994).
4. E. Cucho, P. Marquet, and C. Depeursinge, "Simultaneous amplitude-contrast and quantitative phase-contrast microscopy by numerical reconstruction of Fresnel off-axis holograms," *Appl. Opt.* **38**, 6994–7001 (1999).
5. C. Thomas Jr., T. M. Bahm, L. R. Baylor, P. R. Bingham, S. W. Burns, M. Chidley, L. Dai, R. J. Delahanty, C. J. Doti, A. El-Khashab, R. L. Fisher, J. M. Gilbert, J. S. Goddard, Jr., G. R. Hanson, J. D. Hickson, M. A. Hunt, K. W. Hylton, G. C. John, M. L. Jones, K. R. Macdonald, M. W. Mayo, I. McMackin, D. R. Patek, J. H. Price, D. A. Rasmussen, L. J. Schaefer, T. R. Scheidt, M. A. Schulze, P. D. Schumaker, B. Shen, R. G. Smith, A. N. Su, K. W. Tobin, Jr., W. R. Usry, E. Voelkl, K. S. Weber, P. G. Jones, and R. W. Owen, "Direct to digital holography for semiconductor wafer defect detection and review," in *Design, Process Integration, and Characterization for Microelectronics*, Proc. SPIE **4692**, 180–194 (2002).
6. M. Schulze, M. Hunt, M. Mayo, E. Voelkl, J. Hickson, W. Usry, R. Smith, R. Bryant, and C. Thomas, Jr., "Semiconductor wafer defect detection using digital holography," in *Process and Materials Characterization and Diagnostics in IC Manufacturing II*, Proc. SPIE **5041**, 183–193 (2003).
7. P. Bingham, K. Tobin, G. Hanson, and J. Simpson, "Spatial heterodyne interferometry techniques and applications in semiconductor wafer manufacturing," in *Proceedings of Optical Interferometry XII*, Proc. SPIE **5531**, 289–298 (2004).
8. S. Inouè and K. Spring, *Video Microscopy*, 2nd ed. (Plenum, 1997), pp. 32–37.
9. J. W. Goodman, *Introduction to Fourier Optics*, 2nd ed. (McGraw-Hill, 1996).
10. A. Oppenheim and R. Schaefer, *Discrete-Time Signal Processing* (Prentice-Hall, 1989).